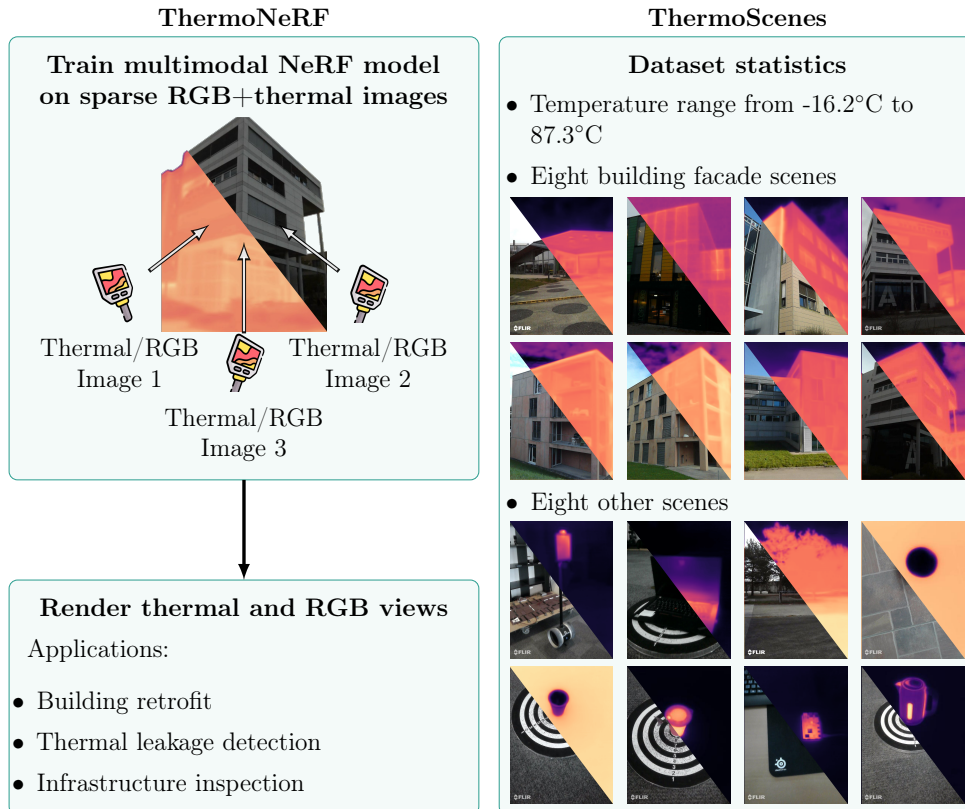


Graphical Abstract

ThermoNeRF: Joint RGB and Thermal Novel View Synthesis for Building Facades using Multimodal Neural Radiance Fields

Mariam Hassan, Florent Forest, Olga Fink, Malcolm Mielle



Highlights

ThermoNeRF: Joint RGB and Thermal Novel View Synthesis for Building Facades using Multimodal Neural Radiance Fields

Mariam Hassan, Florent Forest, Olga Fink, Malcolm Mielle

- We propose ThermoNeRF, a method to synthesize novel RGB+thermal views.
- We introduce ThermoScenes, a novel dataset with 16 scenes (with 8 building facades).
- We show that separating RGB and thermal fields prevents information leakage.
- Joint learning of the density improves density estimations for both modalities.

ThermoNeRF: Joint RGB and Thermal Novel View Synthesis for Building Facades using Multimodal Neural Radiance Fields

Mariam Hassan^a, Florent Forest^a, Olga Fink^a, Malcolm Mielle^b

^a*Intelligent Maintenance and Operations Systems, EPFL, 1015 Lausanne, Switzerland*

^b*Schindler EPFL Lab, 1015 Lausanne, Switzerland*

Abstract

Thermal scene reconstruction holds great potential for various applications, such as analyzing building energy consumption and performing non-destructive infrastructure testing. However, existing methods typically require dense scene measurements and often rely on RGB images for 3D geometry reconstruction, projecting thermal information post-reconstruction. This can lead to inconsistencies between the reconstructed geometry and temperature data and their actual values. To address this challenge, we propose ThermoNeRF, a novel multimodal approach based on Neural Radiance Fields that jointly renders new RGB and thermal views of a scene, and ThermoScenes, a dataset of paired RGB+thermal images comprising 8 scenes of building facades and 8 scenes of everyday objects. To address the lack of texture in thermal images, ThermoNeRF uses paired RGB and thermal images to learn scene density, while separate networks estimate color and temperature data. Unlike comparable studies, our focus is on temperature reconstruction and experimental results demonstrate that ThermoNeRF achieves an average mean absolute error of 1.13°C and 0.41°C for temperature estimation in buildings and other scenes, respectively, representing an improvement of over 50% compared to using concatenated RGB+thermal data as input to a standard NeRF. Code and dataset are available online.

Keywords:

NeRF, thermography, thermal imaging, building, novel view synthesis, building information modeling

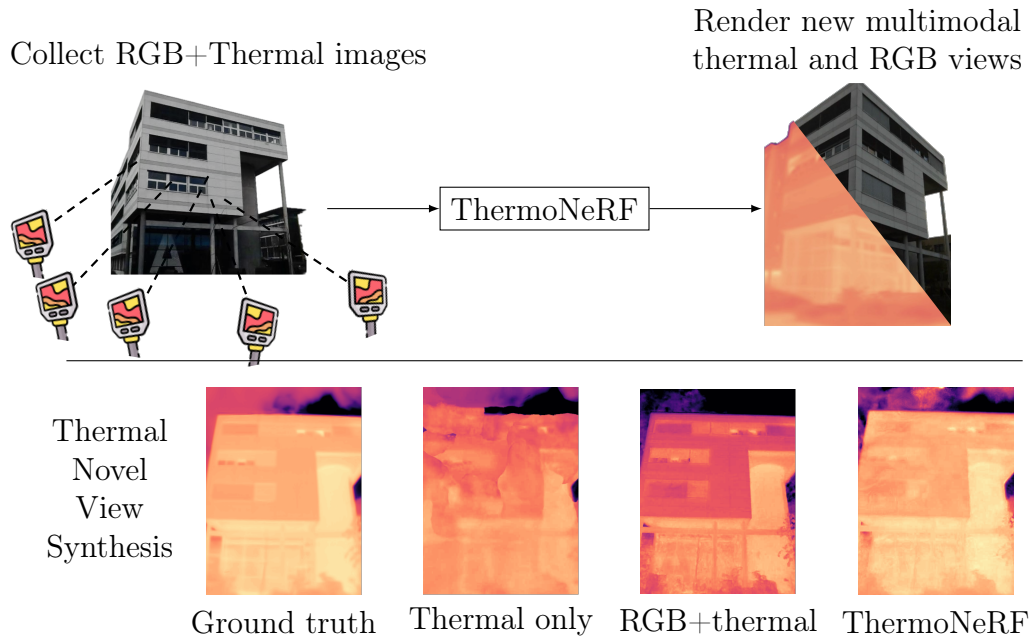


Figure 1: Overview of the capabilities of the proposed ThermoNeRF. It is a multimodal NeRF-based approach using paired thermal and RGB images. ThermoNeRF demonstrates enhanced geometry and thermal information estimation compared to thermal only models which cannot recover the geometry, or RGB+Thermal NeRF models for which information from the RGB image leaks into the temperature of the final rendered view.

1. Introduction

Thermal scene reconstruction offers significant potential for a wide range of applications, including building energy consumption analysis [1], non-destructive testing [2], infrastructure inspection and monitoring [2, 3], and optimization of the cost-effectiveness of building facade retrofit [4]—notably, building facades play a crucial role in regulating the energy flowing in and out of buildings [5]. However, while thermal cameras capture radiation emitted by objects as a function of temperature, thermal images inherently lack texture and exhibit low edge contrast due to scattering and reflection from various surfaces, resulting in an effect known as ghosting [6]. Consequently, thermal images are often not considered during geometric reconstruction, with 3D thermal models predominantly constructed using photogrammetry with large amounts of RGB images [7, 8, 9]. In these models, temperature information is merely projected onto the reconstructed geometry post-reconstruction [10],

leading to discrepancies between the geometry and the temperature data. The development of thermal scene reconstruction algorithms also faces challenges due to the lack of benchmark datasets specifically designed for this task, especially in the context of building facade reconstruction.

Recently, Neural Radiance Fields (NeRFs) [11] have achieved great success in 3D reconstruction and novel view synthesis by learning an implicit representation of a scene from a set of sparse RGB images. While most NeRF models focus on learning from RGB images, they have also been extended to other sensor modalities such as hyperspectral images [12], acoustic signals [13], point clouds [14, 15], or thermal images [16, 17]. However, prior research on NeRF utilizing thermal images has either relied on high-resolution thermal images captured with costly equipment or emphasized the visual quality of the reconstruction in either low-light conditions [18] or against occlusions [16], without prioritizing the precision of the estimated temperature which hinders their practical use in different applications.

To bridge these research gaps, we propose (1) ThermoNeRF (Thermographic NeRF), a multimodal NeRF model capable of rendering unseen views in both RGB and thermal modalities with a focus on temperature rendering quality and not only image quality (see Fig. 1) and (2) ThermoScenes, the first paired RGB+thermal dataset comprising sixteen diverse scenes—eight building facade scenes and eight everyday objects scenes. The design of ThermoNeRF is guided by the specific properties of thermal images. ThermoNeRF uses a shared density MLP that leverages the visual features of the RGB modality to learn the geometry of the scene while ensuring consistency with the thermal measurements. On the other hand, color and thermal information are learned through decoupled MLPs, preventing the influence of colors on the estimated temperatures, and vice-versa. Both the dataset¹ and the code² (including instructions to submit new scenes to the dataset) are available online.

Our contributions are summarized as follows:

- We propose ThermoNeRF, a multimodal NeRF capable of rendering both thermal and RGB views jointly and conduct extensive experiments to validate how ThermoNeRF’s architecture allows the RGB modality to guide the density estimation for thermal reconstruction while preventing

¹<https://doi.org/10.5281/zenodo.10835108>

²<https://github.com/Schindler-EPFL-Lab/thermo-nerf>

information leakage between both modalities, hence leading to accurate temperature estimations.

- We provide ThermoScenes, the first RGB+thermal image dataset for 3D scene reconstruction and novel view synthesis, featuring 16 scenes with diverse temperature ranges and objects, including 8 building facades and 8 everyday object scenes.
- Finally, we present a comprehensive evaluation covering both temperature estimation and reconstruction quality on unseen poses.

Our results demonstrate improved temperature estimation with no loss in reconstruction fidelity when compared to models trained using only thermal images or concatenated RGB+thermal images as input.

2. Related Work

2.1. Thermal Computer Vision

Thermal cameras measure thermal radiation emitted by any matter with a temperature above absolute zero Kelvin. While most practical temperature ranges fall within the infrared (IR) region of the electromagnetic spectrum [19], thermal cameras operate in the mid- to far-IR spectrum, unlike near-infrared (NIR) sensors, which work closer to the visible range. Thermal cameras detect thermal radiations that are scattered and reflected by objects and the environment, resulting in thermal images that are naturally textureless and soft—a phenomenon known as the ghosting effect [6].

While researchers have explored object detection [20] and tracking [21] using infrared sensors, as well as the analysis of thermal images [22, 23, 24], due to their soft and textureless nature, working with thermal images is a challenge [6]. Hence, early studies modeling thermal data predominantly relied on range measurements—e.g. LiDAR [25], depth cameras [26, 27] or both [28]—to construct 3D models, onto which thermal information was subsequently projected. However, those approaches require a time-consuming and error-prone manual calibration of sensor transformations, their precision depends on the accuracy of mapping algorithms, and in the case of depth cameras, are limited by their range. To remove the dependence on range measurements, Maset et al. [7], De Luis-Ruiz et al. [8] use photogrammetry to construct 3D models from RGB images. While these methods achieve high model accuracy, they depend on a dense set of RGB and thermal images.

On the other hand, Chen et al. [29] and Sentenac et al. [30] used thermal images for 3D reconstruction and temperature estimation but their results are limited to thermal images with high contrast and do not generalize to large structures like building facades. Hence, building thermal envelope analysis is usually done by mapping thermal data on existing models [31].

2.2. *NeRF and Multimodality*

Traditional methods in 3D reconstruction, such as Structure from Motion [32] or Multi-View Stereo [33], depend on dense input data and scenes rich in geometric features. The seminal work by Mildenhall et al. [11] introduced NeRF, enabling the learning of implicit representations of 3D scenes from sparse sets of RGB images for novel view synthesis. Subsequent research efforts have extended and refined the NeRF framework, addressing challenges related to scalability [34], level of detail [35, 36] and efficiency [37].

To enhance scene reconstruction, the first multimodal approach incorporated depth data to guide the learning process [38]. However, recent studies have demonstrated that integrating other modalities—e.g. RGB 2D images and LiDAR 3D point clouds [14] or spectral information from filtered RGB inputs [39]—into NeRF can also yield improved scene representations.

Closely related to our work on thermal imaging, Poggi et al. [12] integrates near-infrared and RGB images to create a composite NIR-RGB 3D scene. However, NIR images share similar features with RGB images, as they are closer to the visible spectrum compared to thermal images.

Unlike existing methods that rely on multimodal data with salient visual features, ThermoNeRF combines RGB and thermal features to learn consistent scene geometries across both sensor modalities, while avoiding contamination from each modality in the rendered views.

Concurrently to our work, other studies have investigated the use of NeRFs and thermal imaging [16, 17, 40]. However, they either rely on high-quality thermal images or focus on adverse conditions—such as low-light environments [18]—to enhance the visual quality of generated images, typically evaluated using RGB-specific metrics such as the PSNR, SSIM, and LPIPS. For instance, Xu et al. [18] only evaluate visible light image synthesis, neglecting the quality of the resulting thermal images. In contrast, our work prioritizes the accuracy of predicted temperatures in the synthesized novel views, which is crucial for practical, real-world applications such as thermal modeling of buildings.

2.3. Thermal 3D Reconstruction for Building Retrofit

Both 3D reconstruction and thermal imaging have been employed for building evaluation and retrofit. However, most state-of-the-art methods require either expensive and complex software [4], extensive data-collection and cleaning efforts [41], or a combination of both [42, 43].

Most similar to our work, Ham and Golparvar-Fard [44] uses photogrammetry to reconstruct four indoor scenes and detect condensation issues and thermal resistance of the wall. However, their approach shares the same limitations as the photogrammetry-based methods discussed in Section 2.1.

In conclusion, while both 3D reconstruction and thermal imaging have been employed for building evaluation and retrofit purposes, current state-of-the-art methods often present significant complexities and requirements. Our research tackle those issues by presenting a more practical and accessible approach to thermal modeling of buildings. ThermoNeRF combines the use of sparse data as input (i.e., flexibility in the data collection) and joint multi-modal reconstruction that does not rely on thermal to RGB projection.

3. Preliminary

NeRF [11] learns an implicit scene representation as a continuous 5D vector-valued function, mapping a 3D position $\mathbf{x} = (x, y, z)$ and a viewing direction $\mathbf{d} = (\theta, \phi)$ to a color c and a volume density σ . This mapping is applied along rays projected in space from each pixel of an image captured by a camera at pose (\mathbf{x}, \mathbf{d}) . NeRF comprises two Multi-Layer Perceptron (MLP) networks: one predicts the density based solely on the 3D location, and the other predicts color based on the 3D location and the viewing direction, making the color prediction view-dependent to account for non-Lambertian effects on surfaces. Finally, to reconstruct a view, rays are sampled through the scene, and the color of each ray is rendered using volume rendering techniques.

Nerfacto [45] is a recent extension of NeRF that integrates components from several state-of-the-art models, such as MIP-NeRF [35], MIP-NeRF 360 [46], Instant-NGP [47] and NeRF-W [34], amongst others. The model’s inputs include an additional appearance embedding, which is a per-image embedding that accounts for differences in exposure and lighting conditions across different training views. Furthermore, sinusoidal-based positional encoding is replaced with hash encoding for positions and spherical harmonics

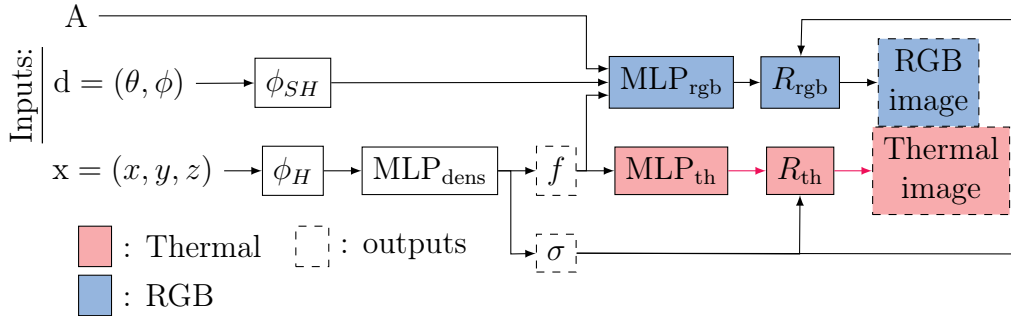


Figure 2: ThermoNeRF architecture; in red are parts of the network related to the generation of thermal images, while blue represents the parts related to the generation of RGB images. The MLP_{th} is only dependent on the intermediate features f as input. A is appearance embeddings that accounts for difference in exposure for RGB images.

for viewing direction. Hence, Nerfacto is defined as follows:

$$\begin{aligned} [\sigma, f] &= \text{MLP}_{\text{dens}}(\phi_H(x)), \\ c &= \text{MLP}_{\text{rgb}}(f, \phi_{SH}(d), A), \end{aligned} \tag{1}$$

where f are intermediate features, c is colors, $\phi_H(\cdot)$ denotes the hash encoding, $\phi_{SH}(\cdot)$ is the spherical harmonics encoding and A represents the appearance embeddings.

Additionally, Nerfacto uses pose refinement to further optimise the poses predicted for every view. It uses a piecewise sampler to balance sampling through the fine details of the scene and the distant views, and a proposal sampler that emphasizes the density regions of the scene which impact reconstruction quality the most. ThermoNeRF extends Nerfacto to allow reconstruction as well as novel view synthesis of thermal and RGB images.

4. ThermoNeRF

In this section, we present ThermoNeRF, a NeRF model capable of learning an implicit scene representation in both thermal and RGB, from a sparse set of RGB and thermal images. To synthesize realistic and accurate RGB and thermal novel views, ThermoNeRF retains geometric features captured by the RGB modality, while ensuring that temperature estimates are independent of scene color variations and details, and that they have a unique value for a given 3D point. Thus, our design choices are guided by two properties of thermal images: 1) thermal images are inherently *soft and textureless*, 2) surface temperatures are *independent of the viewing direction*.

Refer to Fig. 2 for a flowchart of the method; implementation of the model and evaluations can be found online³.

4.1. Thermal Image Rendering

As seen in the thermal images of Fig. 3, the ghosting effect makes thermal images soft and textureless. Consequently, while textures and sharp geometric features in RGB images allow NeRF models to accurately estimate scene density, NeRF struggles to learn densities solely from thermal images—see Fig. 4b for experimental results of training Nerfacto on thermal images only. Therefore, a single density MLP_{dens} is shared by the modalities, enabling the network to construct a geometric representation informed by RGB information while ensuring geometric consistency with the thermal modality. This common density network is defined in the same way as in Section 3:

$$[\sigma, f] = \text{MLP}_{\text{dens}}(\phi_H(\mathbf{x})) \quad (2)$$

Since the aim of ThermoNeRF is to synthesize images that faithfully represent temperature at the surface, details present in the RGB images (such as edges, contrast, texture) should not “leak” into the synthetic thermal views, and colors in the RGB image should not influence the value of the synthesized temperatures in thermal images. Therefore, we propose to use separate MLPs to estimate each modality: MLP_{th} predicts temperatures along each ray, while MLP_{rgb} predicts RGB values.

Furthermore, as depicted in Fig. 3, color information is view-dependent—e.g., due to non-Lambertian effects—which is why, as seen in Eq. (1), MLP_{rgb} takes as input A , and $\phi_{SH}(d)$ to account for view direction. Thermal images are also view-dependent, not due to non-Lambertian effects but due to thermal reflections of nearby heat sources—for example, ceramic, metal, and glass are excellent thermal reflectors. However, in the context of non-destructive testing of infrastructure and infrastructure modeling, it is more interesting to reconstruct an image of the “real” temperature at the surface, rather than a realistic reconstruction of the scene influenced by thermal reflections, i.e. temperature should be invariant with respect to the viewing direction. Thus, MLP_{th} only takes the intermediate features f of MLP_{dens} as input, disregarding A , and ϕ_{SH} .

Formally, ThermoNeRF is defined as follows:

³<https://github.com/Schindler-EPFL-Lab/thermo-nerf>

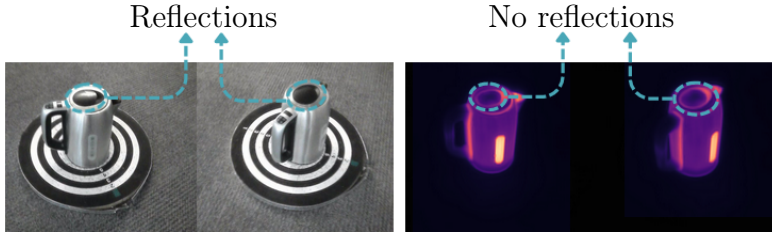


Figure 3: Non-Lambertian effects—i.e. light reflections—present in the RGB images (left) depend on the angle of view and are not present in thermal images (right). Furthermore, textures and edge features in the thermal images are soft due to the ghosting effect, as opposed to the sharpness of the RGB image and its background.

$$\begin{aligned}
 [\sigma, f] &= \text{MLP}_{\text{dens}}(\phi_H(\mathbf{x})), \\
 c &= \text{MLP}_{\text{rgb}}(f, \phi_{SH}(\mathbf{d}), A), \\
 t &= \text{MLP}_{\text{th}}(f),
 \end{aligned} \tag{3}$$

where t denotes the predicted temperature values and A is the appearance embedding.

4.2. Loss Functions

We use separate reconstruction loss functions for each modality. The final reconstruction loss \mathcal{L} is expressed as the sum of the Mean Square Error (MSE) losses of the RGB and thermal outputs, respectively denoted \mathcal{L}_{rgb} and \mathcal{L}_{th} . Similar to Nerfacto, we add the interlevel and distortion losses—respectively $\mathcal{L}_{\text{interl.}}$ and $\mathcal{L}_{\text{dist}}$ —which were initially used in MIP-NeRF 360 [46], to optimize the proposal sampler and to reduce distortions respectively. Therefore, our final loss is defined as follows:

$$\mathcal{L}_{\text{ThermoNeRF}} = \lambda_r \mathcal{L}_{\text{rgb}} + \lambda_t \mathcal{L}_{\text{th}} + \mathcal{L}_{\text{dist}} + \mathcal{L}_{\text{interl.}} \tag{4}$$

While we tried different values for λ_r and λ_t , we empirically found $\lambda_r = \lambda_t = 1$ to be the best value and will thus use it in the rest of this paper.

5. ThermoScenes Dataset

To evaluate RGB+thermal reconstruction and novel view synthesis methods, we have collected ThermoScenes, a new dataset comprising paired RGB and thermal images for 16 scenes (eight building facades and eight other

Table 1: Summary of the collected ThermoScenes dataset showing example views with paired RGB and thermal images, the number of train/test views and the temperature range for each scene, for the eight building scenes (left) and the eight everyday scene (right).

Scene	RGB	Thermal	#views	Temp. range	Scene	RGB	Thermal	#views	Temp. range
Building (Spring)			107 (train) 15 (test)	-62.5°C* 19.7°C	Hot Water Kettle			77 (train) 10 (test)	20.0°C 87.3°C
Exhibition Building			119 (train) 16 (test)	-11.3°C 14.0°C	Melting Ice Cup			85 (train) 12 (test)	0.4°C 25.5°C
Building (Winter)			84 (train) 12 (test)	-15.7°C 15.6°C	Frozen Ice Cup			133 (train) 19 (test)	-16.2°C 23.1°C
Dorm 1			100 (train) 50 (test)	-22.1°C* 24.6°C	Raspberry Pi			111 (train) 15 (test)	22.3°C 41.8°C
Dorm 2			73 (train) 10 (test)	-8.4°C 11.8°C	Double Robot			83 (train) 11 (test)	21.0°C 29.3°C
MED building			93 (train) 46 (test)	-25.2°C* 37.5°C	Heated Water Cup			95 (train) 13 (test)	23.8°C 68.6°C
INR building			111 (train) 40 (test)	-35.5°C* 45.6°C	Trees			73 (train) 10 (test)	-8.4°C 11.8°C
BI building			131 (train) 50 (test)	-0.03°C 19.2°C	Laptop			97 (train) 50 (test)	19.18°C 47.92°C

*Due to the variations of atmospheric radiation in the sky, the readings of thermal cameras are subject to systematic inaccuracies [48] and the measurements are outside the camera’s operating range. We make available the raw data but, in our experiments, the temperature values under the minimum of the operating range of the camera (-20°C) are clipped to -20°C.

everyday scenes) with diverse temperature ranges. A FLIR One Pro LT [49]—a dual RGB and thermal camera mounted on an iPhone and capable of simultaneously capturing aligned pairs of RGB and thermal images—was used to collect the data. The FLIR One Pro LT thermal camera operates within a range of -20 °C to 120 °C, with a thermal accuracy of ± 3 °C. In our study, evaluating the quality of 3D thermal reconstruction requires not only understanding the thermal accuracy but also the thermal precision of the camera. We assess the precision to be approximately ± 0.14 °C. To calculate the precision of our thermal camera, we fix the camera at a position and capture 20 consecutive images of a RaspberryPi connected to power for at

least 10 minutes to ensure thermal stability. Our precision is then the average standard deviation of the temperatures of each pixel across the 20 images.

Furthermore, the FLIR software generates thermal images by overlaying thermal information onto RGB features—such as edges—using Multi-Spectral Dynamic Imaging (MSX) [50]. Instead, we provide and use raw thermal data extracted from MSX images using the FLIR Image Extractor library [51].

Table 1 provides a summary of the scenes comprising the ThermoScenes dataset, where each scene is illustrated by two example views in RGB and thermal respectively. The test set for each scene is uniformly sampled across the collected camera poses. The minimum and maximum measured temperatures are also reported. It should be noted that in the Building (spring), Dorm 1, MED, and INR building scenes, the sensor outputs values outside of its operating range due to the variations of atmospheric radiation in the sky, where the readings of thermal cameras are subject to systematic inaccuracies [48]. Given our focus on the object of interest—the building facade—we limit these values to the minimum of the operating range of the camera (-20°C) in our experiments. However, for other applications where more precise temperature estimates for the sky might be needed, we provide the raw data to allow for potential post-processing (see Kruczek [48] and Zhao et al. [52]).

ThermoScenes is publicly available⁴ and we plan to gradually increase the size of the dataset. A tutorial on how to collect, process, and train data on ThermoNeRF has also been released.⁵

6. Experiments

We conduct a comprehensive evaluation of rendered novel views using ThermoScenes. This section details the evaluation metrics, compares baselines, and discusses results.

6.1. Evaluation Metrics

Temperature Metrics. We assess the accuracy of the rendered temperatures by calculating the Mean Absolute Error (MAE). Given that thermal images often display uniform temperature distributions outside the regions of interest (ROI), calculating the MAE across the entire image may disproportionately

⁴<http://dx.doi.org/10.5281/zenodo.10835108>

⁵https://github.com/Schindler-EPFL-Lab/thermo-nerf/blob/main/thermo_scenes/docs/Collect_new_dataset.md

Table 2: Quantitative comparison of our method (ThermoNeRF) versus Nerfacto_{th} and Nerfacto_{rgb+th} on thermal novel view synthesis across the building scenes in ThermoScenes.

Metric	Method	Building (Spring)	Building (Winter)	Exhibition Building	MED	Dorm 1	Dorm 2	INR	BI	Avg
PSNR ↑	Nerfacto _{th}	20.30	22.80	23.88	19.26	18.65	19.42	18.8	22.95	20.77
	Nerfacto _{rgb+th}	20.60	28.47	27.74	20.58	32.44	26.64	21.05	27.15	26.24
	ThermoNeRF	26.63	28.75	33.79	22.04	34.10	29.94	22.45	28.83	28.62
SSIM ↑	Nerfacto _{th}	0.91	0.87	0.94	0.93	0.92	0.92	0.87	0.85	0.90
	Nerfacto _{rgb+th}	0.89	0.89	0.95	0.93	0.95	0.95	0.86	0.86	0.91
	ThermoNeRF	0.92	0.88	0.97	0.93	0.96	0.95	0.88	0.87	0.92
MAE _{roi} °C ↓	Nerfacto _{th}	6.36	1.80	1.29	4.95	4.37	3.93	1.81	1.70	3.09
	Nerfacto _{rgb+th}	6.54	0.86	1.00	3.62	0.63	0.77	1.31	1.04	1.79
	ThermoNeRF	1.88	0.66	0.31	3.10	0.38	0.75	1.28	0.74	1.04
MAE °C ↓	Nerfacto _{th}	6.74	1.87	1.56	4.62	4.06	3.65	2.16	1.81	3.11
	Nerfacto _{rgb+th}	6.59	0.89	0.97	3.80	0.68	3.65	1.63	1.00	2.17
	ThermoNeRF	2.40	0.76	0.35	3.38	0.46	0.77	0.93	0.76	1.13

emphasize the ambient background temperature. From an application standpoint, the temperature of the ROI (e.g., the building facade) is crucial for temperature assessment [53]. Therefore, we also report the MAE_{roi}, the MAE computed over the region of interest. We use Otsu’s method [54] to determine the optimal threshold that distinguishes the ROI pixels from the background in thermal images. We also report the standard image quality metrics to evaluate the reconstruction quality for RGB and thermal images.

Image Quality Metrics. We report the commonly used image quality metrics Peak-Signal-to-Noise-Ratio (PSNR) [55] and Structural Similarity Metric (SSIM) [56] for both thermal and RGB modalities. For the RGB views, we also include the Learned Perceptual Image Patch Similarity (LPIPS) [57]; since the LPIPS is specifically designed to evaluate the human-perceived similarity for RGB images, we do not include it for thermal images evaluation.

Note that most works in RGB+thermal novel view synthesis have focused on evaluating only image quality metrics, either solely for the RGB modality [18, 40]—highlighting the visual improvement in RGB brought by the use of thermal images—or on both RGB and thermal modalities [16, 17]. In both cases, the visual quality of the generated images is being evaluated. However, the differences between the estimated and ground-truth temperature values is not measured nor analyzed. In the present work, we rather focus on temperature metrics—while ensuring good visual quality—as accurately reconstructing the surface temperature is crucial for real-world applications

Table 3: Quantitative comparison of our method (ThermoNeRF) versus Nerfacto_{th} and Nerfacto_{rgb+th} on thermal novel view synthesis across the non-building scenes in ThermoScenes.

Metric	Method	Heated Water Cup	Heated Water Kettle	Freezing Ice Cup	Melting Ice Cup	Double Robot	RPi	Laptop	Trees	Avg
PSNR ↑	Nerfacto _{th}	23.68	29.25	23.34	18.50	10.49	18.08	18.28	20.91	20.32
	Nerfacto _{rgb+th}	29.76	31.80	22.9	32.70	29.82	24.30	24.28	31.48	28.38
	ThermoNeRF	32.05	34.04	30.67	32.24	30.75	31.80	25.40	31.07	31.00
SSIM ↑	Nerfacto _{th}	0.71	0.89	0.95	0.93	0.45	0.71	0.65	0.92	0.78
	Nerfacto _{rgb+th}	0.83	0.91	0.96	0.98	0.89	0.82	0.73	0.94	0.88
	ThermoNeRF	0.92	0.94	0.97	0.98	0.95	0.96	0.74	0.94	0.92
MAE _{roi} °C ↓	Nerfacto _{th}	13.57	5.18	6.75	12.27	2.85	4.82	11.33	1.60	7.30
	Nerfacto _{rgb+th}	5.35	3.25	10.33	1.26	1.06	1.62	0.54	0.31	2.96
	ThermoNeRF	2.10	2.76	3.26	1.57	0.91	1.28	0.43	0.25	1.57
MAE °C ↓	Nerfacto _{th}	1.82	4.19	1.67	1.97	5.33	2.25	0.54	1.49	2.41
	Nerfacto _{rgb+th}	0.87	1.54	2.01	0.46	0.55	1.15	0.33	0.34	0.91
	ThermoNeRF	0.53	0.71	0.57	0.29	0.34	0.27	0.28	0.33	0.41

such as building envelope analysis for retrofit purposes.

6.2. Baselines

We conduct experiments to evaluate (1) the necessity of multimodality, as thermal images alone cannot accurately estimate the scene density due to lack of texture details, and (2) the decoupling of the RGB and thermal modalities, stemming from the physical independence between temperature and color information. Given that ThermoNeRF is based on Nerfacto, we define two baseline methods derived from Nerfacto: Nerfacto_{th} and Nerfacto_{rgb+th}.

Nerfacto_{th} is trained with thermal inputs only and processes thermal images as single-channel grayscale images through Nerfacto’s standard pipeline. It highlights the importance of incorporating the RGB modality.

Nerfacto_{rgb+th} takes both RGB and thermal modalities as inputs by concatenating them into four-channel images and optimizes the concatenated RGB-thermal images without employing separate MLPs for optimizing each modality. Tests against Nerfacto_{rgb+th} highlights the importance of disjoint optimization of the modalities.

6.3. Implementation Details

We use 2-layer MLP with width 64 and 1 output dimension for MLP_{th} and MLP_{dens}. For MLP_{rgb}, we use 3-layer MLP with width 64 and 3 output dimensions. We use ReLU activation function for all MLPs and Sigmoid

function for the head of MLP_{th} and MLP_{rgb} . We use the default NeRFstudio [58] settings for the hash encoder which has a minimum and maximum resolution of 16 and 1024 respectively and 2 features per level. Additionally, we use the default settings of the spherical harmonic encoding with 4 spherical harmonic levels. All details are available in our code repository⁶.

We train ThermoNeRF as well as our baselines for 30k iterations with 4096 rays per batch. We use a learning rate of 10^{-2} with exponential decay decreasing the learning rate by an order of magnitude to 10^{-3} . The total training time is around 40 minutes using a single T4 GPU.

6.4. Thermal View Synthesis

Table 3 and Table 2 provide a comparative analysis of our method’s performance for novel view synthesis for the thermal modality on the ThermoScenes dataset.

With an average MAE of 1.13°C on building scenes and 0.41°C on other scenes, ThermoNeRF significantly outperforms $\text{Nerfacto}_{\text{rgb+th}}$ (2.17°C and 0.91°C) and $\text{Nerfacto}_{\text{th}}$ (3.11°C and 2.41°C). When trained on thermal images alone, $\text{Nerfacto}_{\text{th}}$ fails to learn an accurate representation of the scene (as visible in Fig. 4b) and has the lowest image quality and temperature estimation results. On the other hand, thanks to the concatenation of RGB and thermal information, $\text{Nerfacto}_{\text{rgb+th}}$ obtains better results than $\text{Nerfacto}_{\text{th}}$: MAE_{roi} of 1.79°C , against 3.09°C for $\text{Nerfacto}_{\text{th}}$ on building scenes, and 2.96°C against 7.30°C on other scenes. However, the estimated temperatures are impacted by the joint optimization of both modalities in the same MLP, as evidenced in Fig. 5 where the error in temperature prediction is high on the ROI. On the contrary, the average MAE_{roi} and MAE for ThermoNerf mark a significant improvement over the other methods (for the MAE 1.13°C on building scenes and 1.57°C for others and for the MAE_{roi} 1.04°C for buildings and 1.57°C for others).

Additionally, we visually compare examples of test views rendered by each of the baseline methods as well as by ThermoNeRF (see Fig. 4). We observe noisy renderings with $\text{Nerfacto}_{\text{th}}$, while $\text{Nerfacto}_{\text{rgb+th}}$ generates sensible reconstructions of the geometry. However, temperature predictions of $\text{Nerfacto}_{\text{rgb+th}}$ are influenced by the RGB modality, leading to biased temperature values, sharper edges compared to the ground truth, and elements

⁶<https://github.com/Schindler-EPFL-Lab/thermo-nerf>

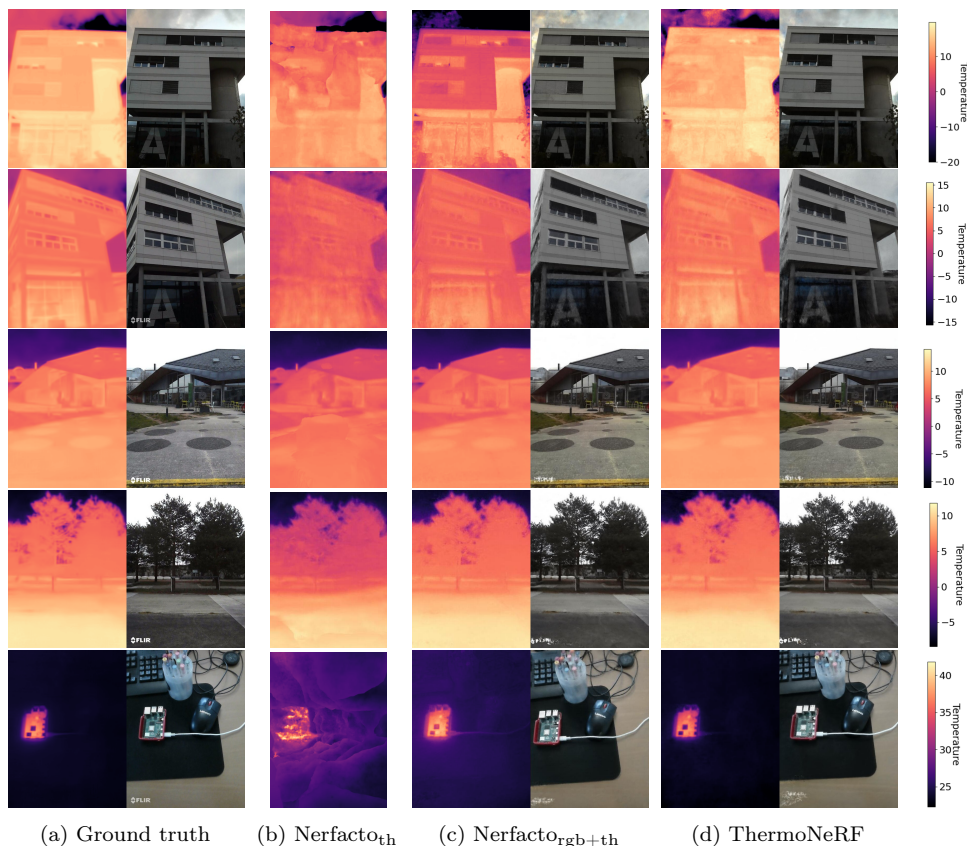


Figure 4: Comparison of examples of thermal and RGB renderings of unseen poses for the four outdoor scenes (top to bottom rows): Building (Spring), Building (Winter), Exhibition Building, Trees, and Raspberry pi. ThermoNeRF is closest to the ground-truth thermal image, while preserving RGB quality.

from RGB images that are visible in the synthesized thermal images. For example, in Fig. 4, for each Nerfacto_{rgb+th} image, the colors have leaked into the thermal images and buildings are warmer than the ground truth. While the building (spring) scene (top-row of Fig. 4) looks sharper when synthesized using Nerfacto_{rgb+th} compared to ThermoNeRF, in Fig. 5 top left row, one can see that the sharpness of the image comes with a high error rate on the temperature rendering—with a MAE of 8.32° as opposed to 1.71° for ThermoNeRF. Another example of detail leaking from the RGB into the thermal images can be seen in Fig. 5 and Fig. 6, where edges and structures are corresponding to high errors in Nerfacto_{rgb+th}.

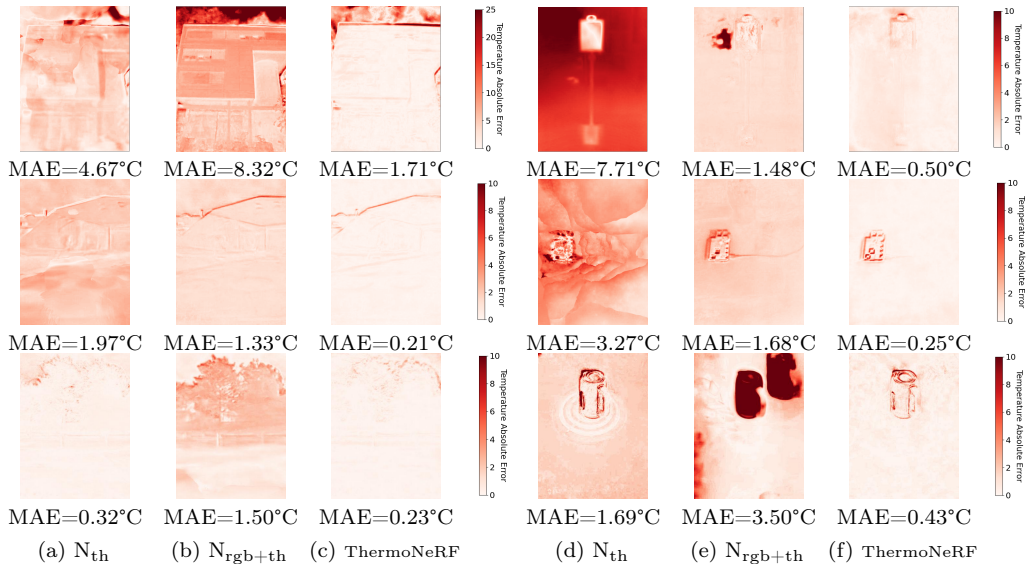


Figure 5: Per-pixel absolute errors in temperature estimation for renderings of unseen poses for three outdoor scenes: (left top to bottom) Building Spring, Exhibition Building and Trees, and three indoor scenes: (right top to bottom) Double Robot, RaspberryPi, and Heated Water Kettle. We observe fewer errors on ThermoNeRF than the baselines. Note that $N_{\text{rgb+th}}$ stands for $\text{Nerfacto}_{\text{rgb+th}}$.

For in-detail qualitative evaluation of the results, the per-pixel absolute errors in temperature prediction is visualized in Fig. 5. One can see that the highest errors for all models are observed at the edges, due to the ghosting effect of thermal images leading to blurry edges. It should be noted that ThermoNeRF exhibits the best thermal prediction results while $\text{Nerfacto}_{\text{th}}$ shows the worst thermal predictions. $\text{Nerfacto}_{\text{rgb+th}}$ shows higher errors across the scenes than ThermoNeRF due to the contamination of the thermal information by the RGB modality.

Furthermore, cloudy skies are known to provide ideal conditions for infrared measurements outdoors, since the measured object is protected against solar radiation. This fact is supported by the comparison of the thermal image synthesis of Building Spring (top-left) and the Exhibition Building scenes. During measurements, the Building Spring scene’s sky is a mix of clear and cloudy images leading to more noise in the image synthesis than the second scene that consists of a uniform cloudy sky.

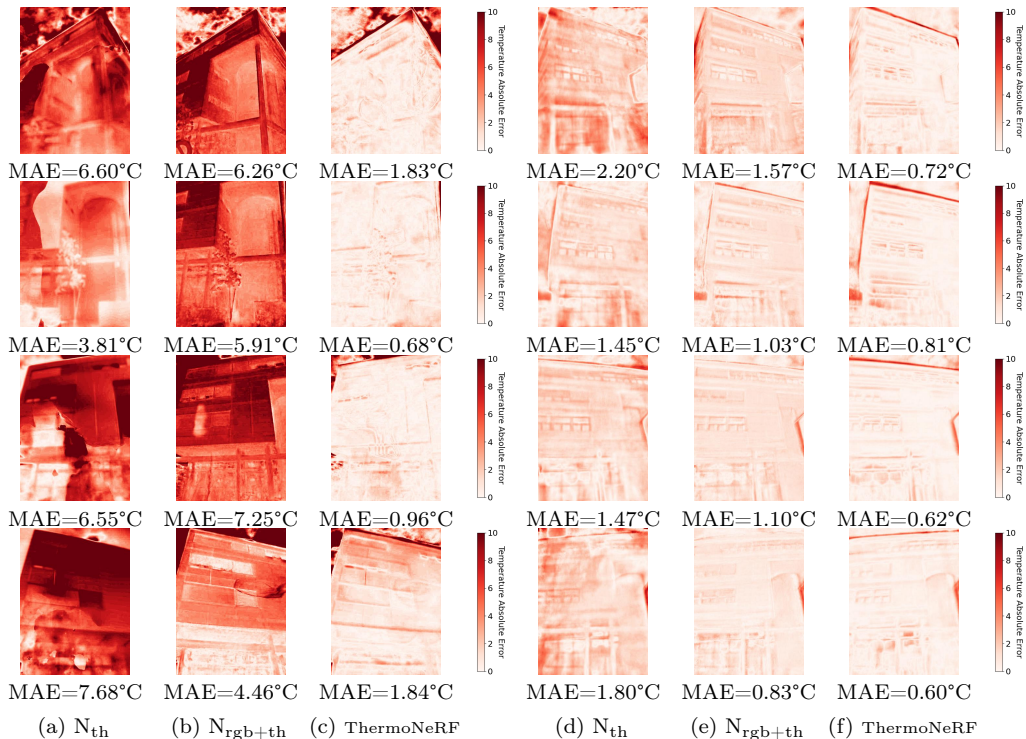


Figure 6: Comparison of per-pixel absolute errors in temperature estimation for renderings of different unseen poses for two scenes: Building Spring (left) and Building Winter (right). We observe fewer errors on ThermoNeRF (highlighted in green) than the baselines. Note that N_{rgb+th} stands for Nerfacto $_{rgb+th}$.

6.5. RGB View Synthesis

We investigate whether there is a significant degradation in the quality of RGB views compared with the standard Nerfacto trained only on the RGB inputs. Table 4 and Table 5 summarize the results, showing little to no degradation in the quality of the RGB views. Indeed, the differences between the PSNR, SSIM and LPIPS of Nerfacto and ThermoNeRF in RGB are respectively -0.09 , -0.01 and -0.01 on building scenes, and -0.63 , -0.03 and 0.005 on other scenes. The results support that using ThermoNeRF leads to higher accuracy in temperature without a significant degradation in the quality of the reconstructed RGB views. Thus, our approach effectively learns to model 3D scenes across both RGB and thermal modalities, making it suitable for various downstream tasks including building retrofit, energy consumption analysis and non-destructive infrastructure inspection.

Table 4: Quantitative comparison of the rendered RGB views between ThermoNeRF and a Nerfacto trained only with RGB across the buildings in ThermoScenes. There is no observed significant degradation of the quality of RGB views due to the multimodal learning.

Metric	Method	Building (Spring)	Building (Winter)	Exhibition Building	MED	Dorm 1	Dorm 2	INR	BI	Avg
PSNR \uparrow	Nerfacto (RGB)	19.88	20.02	22.18	17.53	19.13	19.11	14.17	20.38	19.06
	ThermoNeRF	19.30	19.74	22.81	16.40	18.70	19.20	13.39	20.90	18.80
	Difference	-0.58	-0.28	+0.83	-0.13	-0.43	+0.09	-0.78	+0.52	-0.09
SSIM \uparrow	Nerfacto (RGB)	0.64	0.62	0.64	0.43	0.57	0.61	0.39	0.65	0.57
	ThermoNeRF	0.63	0.61	0.66	0.38	0.55	0.61	0.35	0.69	0.56
	Difference	-0.02	-0.01	+0.02	-0.05	-0.02	+0.00	-0.04	+0.04	-0.01
LPIPS \downarrow	Nerfacto (RGB)	0.24	0.34	0.24	0.32	0.17	0.19	0.59	0.27	0.29
	ThermoNeRF	0.27	0.34	0.24	0.38	0.19	0.22	0.61	0.28	0.32
	Difference	+0.03	0.00	0.00	-0.06	-0.02	-0.03	-0.02	-0.01	-0.01

Table 5: Quantitative comparison of the rendered RGB views between ThermoNeRF and Nerfacto trained only with RGB across the everyday life scenes in ThermoScenes. There is no significant degradation by the multimodal learning.

Metric	Method	Heated Water Cup	Heated Water Kettle	Freezing Ice Cup	Melting Ice Cup	Double Robot	Raspberry Pi	Trees	Laptop	Avg
PSNR \uparrow	Nerfacto (RGB)	18.11	23.00	24.71	17.97	19.05	19.36	20.37	19.3	20.23
	ThermoNeRF	18.16	21.05	25.69	16.20	19.02	19.07	18.67	18.83	19.58
	Difference	+0.05	-1.95	+0.98	-1.77	-0.03	-0.29	-1.61	-0.47	-0.63
SSIM \uparrow	Nerfacto (RGB)	0.53	0.75	0.73	0.52	0.65	0.73	0.67	0.61	0.65
	ThermoNeRF	0.56	0.60	0.77	0.43	0.65	0.72	0.59	0.61	0.62
	Difference	+0.03	-0.15	+0.04	-0.09	0.00	-0.01	-0.08	0	-0.03
LPIPS \downarrow	Nerfacto (RGB)	0.25	0.23	0.42	0.17	0.28	0.18	0.32	0.21	0.26
	ThermoNeRF	0.25	0.24	0.37	0.18	0.30	0.19	0.35	0.22	0.26
	Difference	0.00	+0.01	-0.05	+0.01	+0.02	+0.01	+0.03	+0.01	0.005

7. Conclusion

In this work, we propose ThermoNeRF, a novel multimodal approach that leverages NeRF to render novel RGB and thermal views of a scene. Our method facilitates thermal analysis of buildings by using a sparse set of images captured from various angles around the structure. We curated a new dataset specifically tailored for RGB+thermal scene reconstruction, and our experimental results show that ThermoNeRF excels at synthesizing thermal images. It achieves an average MAE of 0.41°C on indoor scenes and 1.13°C on buildings, representing respective improvements of over 55% and 48% compared to the baseline approach that concatenates RGB and thermal

modalities. A potential limitation of our method is its reliance on paired RGB and thermal images, as collecting such data requires precise camera calibration to ensure accurate alignment between the two modalities, which can pose practical challenges. To address this, future work will focus on developing techniques to train ThermoNeRF using unpaired RGB and thermal image data. We believe our method paves the way for new opportunities in thermal building reconstruction. For instance, future models could analyze ThermoNeRF's outputs to detect failures in HVAC systems, piping, or electrical networks. We leave these exciting possibilities for future exploration.

Acknowledgements

We sincerely thank Jiarui Yu and Juliette Parchet for helping with the data collection and for reporting the results of ThermoNeRF on those datasets. We would also like to thank Ali Waseem for running some of the experiments.

This research was supported by Innosuisse - Swiss Innovation Agency, Innosuisse Grant n° **105.237.1 IP-ICT** titled **Insulated: integrated solution for lean and abridged thermal evaluation with digital twins** in collaboration with Schindler AG.

References

- [1] Y. Ham, M. Golparvar-Fard, An automated vision-based method for rapid 3d energy performance modeling of existing buildings using thermal and digital imagery, *Advanced Engineering Informatics* 27 (2013) 395–409. URL: <https://www.sciencedirect.com/science/article/pii/S147403461300027X>. doi:<https://doi.org/10.1016/j.aei.2013.03.005>.
- [2] R. Gade, T. Moeslund, Thermal cameras and applications: A survey, *Machine Vision and Applications* 25 (2014) 245–262. doi:[10.1007/s00138-013-0570-5](https://doi.org/10.1007/s00138-013-0570-5).
- [3] H. Kim, N. Lamichhane, C. Kim, R. Shrestha, Innovations in building diagnostics and condition monitoring: A comprehensive review of infrared thermography applications, *Buildings* 13 (2023). doi:[10.3390/buildings13112829](https://doi.org/10.3390/buildings13112829).

- [4] Y. Ham, M. Golparvar-Fard, Three-dimensional thermography-based method for cost-benefit analysis of energy efficiency building envelope retrofits, *Journal of Computing in Civil Engineering* 29 (2015) B4014009.
- [5] I. Nardi, E. Lucchi, T. de Rubeis, D. Ambrosini, Quantification of heat energy losses through the building envelope: A state-of-the-art analysis with critical and comprehensive review on infrared thermography, *Building and Environment* 146 (2018) 190–205. doi:10.1016/j.buildenv.2018.09.050.
- [6] F. Bao, S. Jape, A. Schramka, J. Wang, T. E. McGraw, Z. Jacob, Why are thermal images blurry, 2023. arXiv:2307.15800.
- [7] E. Maset, A. Fusiello, F. Crosilla, R. Toldo, D. Zorzetto, Photogrammetric 3d building reconstruction from thermal images, *ISPRS Annals of the Photogrammetry, Remote Sensing and Spatial Information Sciences IV-2-W3* (2017) 25–32. URL: <https://isprs-annals.copernicus.org/articles/IV-2-W3/25/2017/>. doi:10.5194/isprs-annals-IV-2-W3-25-2017, conference Name: International Conference on Unmanned Aerial Vehicles in Geomatics (Volume IV-2/W3) - 4–7 September 2017, Bonn, Germany Publisher: Copernicus GmbH.
- [8] J. M. De Luis-Ruiz, J. Sedano-Cibrián, R. Pérez-Álvarez, R. Pereda-García, R. B. Salas-Menocal, Generation of 3d thermal models for the analysis of energy efficiency in buildings, in: F. Cavas-Martínez, M. D. Marín Granados, R. Mirálbes Buil, O. D. de Cózar-Macías (Eds.), *Advances in Design Engineering III*, Springer International Publishing, Cham, 2023, pp. 741–754.
- [9] M. Martin, A. Chong, F. Biljecki, C. Miller, Infrared thermography in the built environment: A multi-scale review, *Renewable and Sustainable Energy Reviews* 165 (2022) 112540. doi:<https://doi.org/10.1016/j.rser.2022.112540>.
- [10] A. Ramón, A. Adán, F. Javier Castilla, Thermal point clouds of buildings: A review, *Energy and Buildings* 274 (2022) 112425. URL: <https://www.sciencedirect.com/science/article/pii/S0378778822005965>. doi:<https://doi.org/10.1016/j.enbuild.2022.112425>.

- [11] B. Mildenhall, P. P. Srinivasan, M. Tancik, J. T. Barron, R. Ramamoorthi, R. Ng, Nerf: Representing scenes as neural radiance fields for view synthesis, in: ECCV, 2020.
- [12] M. Poggi, P. Z. Ramirez, F. Tosi, S. Salti, S. Mattoccia, L. D. Stefano, Cross-Spectral Neural Radiance Fields, in: 2022 International Conference on 3D Vision (3DV), 2022, pp. 606–616. URL: <https://ieeexplore.ieee.org/abstract/document/10044414>. doi:10.1109/3DV57658.2022.00071, iSSN: 2475-7888.
- [13] C. Chen, A. Richard, R. Shapovalov, V. K. Ithapu, N. Neverova, K. Grauman, A. Vedaldi, Novel-view acoustic synthesis, in: Proceedings of the IEEE/CVF Conference on Computer Vision and Pattern Recognition, 2023.
- [14] H. Zhu, Y. Sun, C. Liu, L. Xia, J. Luo, N. Qiao, R. Nevatia, C. Kuo, Multimodal Neural Radiance Field, in: 2023 IEEE International Conference on Robotics and Automation (ICRA), 2023, pp. 9393–9399. doi:10.1109/ICRA48891.2023.10160388.
- [15] J. Zhang, F. Zhang, S. Kuang, L. Zhang, Nerf-lidar: Generating realistic lidar point clouds with neural radiance fields, in: AAAI Conference on Artificial Intelligence (AAAI), 2024.
- [16] Y. Y. Lin, X.-Y. Pan, S. Fridovich-Keil, G. Wetzstein, Thermalnerf: Thermal radiance fields, in: 2024 IEEE International Conference on Computational Photography (ICCP), IEEE, 2024, pp. 1–12.
- [17] M. Özer, M. Weiherer, M. Hundhausen, B. Egger, Exploring multi-modal neural scene representations with applications on thermal imaging, arXiv preprint arXiv:2403.11865 (2024).
- [18] J. Xu, M. Liao, K. R. Prabhakar, V. M. Patel, Leveraging thermal modality to enhance reconstruction in low-light conditions, in: European Conference on Computer Vision, 2024. URL: <https://arxiv.org/abs/2403.14053>.
- [19] L. Hu, M. Delichatsios, Thermal Radiation, Springer International Publishing, Cham, 2019, pp. 1–8. URL: https://doi.org/10.1007/978-3-319-51727-8_78-1. doi:10.1007/978-3-319-51727-8_78-1.

- [20] C. Devaguptapu, N. Akolekar, M. M Sharma, V. N Balasubramanian, Borrow from anywhere: Pseudo multi-modal object detection in thermal imagery, in: Proceedings of the IEEE/CVF Conference on Computer Vision and Pattern Recognition Workshops, 2019, pp. 0–0.
- [21] A. Berg, J. Ahlberg, M. Felsberg, A thermal object tracking benchmark, in: 2015 12th IEEE International Conference on Advanced Video and Signal Based Surveillance (AVSS), IEEE, 2015, pp. 1–6.
- [22] O. Janssens, R. Van de Walle, M. Loccufer, S. Van Hoecke, Deep learning for infrared thermal image based machine health monitoring, IEEE/ASME Transactions on Mechatronics 23 (2017) 151–159.
- [23] Q. Luo, B. Gao, W. L. Woo, Y. Yang, Temporal and spatial deep learning network for infrared thermal defect detection, Ndt & E International 108 (2019) 102164.
- [24] S. Liu, M. Gao, V. John, Z. Liu, E. Blasch, Deep learning thermal image translation for night vision perception, ACM Transactions on Intelligent Systems and Technology (TIST) 12 (2020) 1–18.
- [25] S. Lagüela, J. Martínez, J. Armesto, P. Arias, Energy efficiency studies through 3D laser scanning and thermographic technologies, Energy and Buildings 43 (2011) 1216–1221. URL: <https://www.sciencedirect.com/science/article/pii/S0378778811000041>. doi:10.1016/j.enbuild.2010.12.031.
- [26] S. Vidas, P. Moghadam, Heatwave: A handheld 3d thermography system for energy auditing, Energy and Buildings 66 (2013) 445–460. URL: <https://www.sciencedirect.com/science/article/pii/S0378778813004180>. doi:<https://doi.org/10.1016/j.enbuild.2013.07.030>.
- [27] S. Schramm, P. Osterhold, R. Schmoll, A. Kroll, Combining modern 3D reconstruction and thermal imaging: generation of large-scale 3D thermograms in real-time, Quantitative InfraRed Thermography Journal 19 (2022) 295–311. URL: <https://doi.org/10.1080/17686733.2021.1991746>. doi:10.1080/17686733.2021.1991746, publisher: Taylor & Francis _eprint: <https://doi.org/10.1080/17686733.2021.1991746>.

- [28] I. Campione, F. Lucchi, N. Santopuoli, L. Seccia, 3D Thermal Imaging System with Decoupled Acquisition for Industrial and Cultural Heritage Applications, *Applied Sciences* 10 (2020) 828. URL: <https://www.mdpi.com/2076-3417/10/3/828>. doi:10.3390/app10030828, number: 3 Publisher: Multidisciplinary Digital Publishing Institute.
- [29] C.-Y. Chen, C.-H. Yeh, B. R. Chang, J.-M. Pan, 3D Reconstruction from IR Thermal Images and Reprojective Evaluations, *Mathematical Problems in Engineering* 2015 (2015) e520534. URL: <https://www.hindawi.com/journals/mpe/2015/520534/>. doi:10.1155/2015/520534, publisher: Hindawi.
- [30] T. Sentenac, F. Bugarin, B. Ducarouge, M. Devy, Automated thermal 3D reconstruction based on a robot equipped with uncalibrated infrared stereovision cameras, *Advanced Engineering Informatics* 38 (2018) 203–215. URL: <https://www.sciencedirect.com/science/article/pii/S1474034617305724>. doi:10.1016/j.aei.2018.06.008.
- [31] W. Natephra, A. Motamedi, N. Yabuki, T. Fukuda, Integrating 4d thermal information with bim for building envelope thermal performance analysis and thermal comfort evaluation in naturally ventilated environments, *Building and Environment* 124 (2017) 194–208. URL: <https://www.sciencedirect.com/science/article/pii/S0360132317303499>. doi:<https://doi.org/10.1016/j.buildenv.2017.08.004>.
- [32] J. L. Schonberger, J.-M. Frahm, Structure-from-motion revisited, in: *Proceedings of the IEEE Conference on Computer Vision and Pattern Recognition (CVPR)*, 2016.
- [33] J. L. Schönberger, E. Zheng, J.-M. Frahm, M. Pollefeys, Pixelwise view selection for unstructured multi-view stereo, in: *Computer Vision–ECCV 2016: 14th European Conference, Amsterdam, The Netherlands, October 11–14, 2016, Proceedings, Part III 14*, Springer, 2016, pp. 501–518.
- [34] R. Martin-Brualla, N. Radwan, M. S. Sajjadi, J. T. Barron, A. Dosovitskiy, D. Duckworth, Nerf in the wild: Neural radiance fields for unconstrained photo collections, in: *Proceedings of the IEEE/CVF Conference on Computer Vision and Pattern Recognition*, 2021, pp. 7210–7219.

- [35] J. T. Barron, B. Mildenhall, M. Tancik, P. Hedman, R. Martin-Brualla, P. P. Srinivasan, Mip-nerf: A multiscale representation for anti-aliasing neural radiance fields, ICCV (2021).
- [36] J. T. Barron, B. Mildenhall, D. Verbin, P. P. Srinivasan, P. Hedman, Zip-nerf: Anti-aliased grid-based neural radiance fields, ICCV (2023).
- [37] A. Yu, R. Li, M. Tancik, H. Li, R. Ng, A. Kanazawa, Plenotrees for real-time rendering of neural radiance fields, in: Proceedings of the IEEE/CVF International Conference on Computer Vision, 2021, pp. 5752–5761.
- [38] K. Deng, A. Liu, J.-Y. Zhu, D. Ramanan, Depth-supervised nerf: Fewer views and faster training for free, 2022 IEEE/CVF Conference on Computer Vision and Pattern Recognition (CVPR) (2021) 12872–12881. URL: <https://api.semanticscholar.org/CorpusID:235743051>.
- [39] J. Li, Y. Li, C. Sun, C. Wang, J. Xiang, Spec-NeRF: Multi-spectral Neural Radiance Fields, 2023. URL: <http://arxiv.org/abs/2310.12987>. doi:10.48550/arXiv.2310.12987, arXiv:2310.12987 [cs, eess].
- [40] T. Ye, Q. Wu, J. Deng, G. Liu, L. Liu, S. Xia, L. Pang, W. Yu, L. Pei, Thermal-nerf: Neural radiance fields from an infrared camera, arXiv preprint arXiv:2403.10340 (2024).
- [41] D. Bulatov, D. Frommholz, B. Kottler, K. Qui, E. Strauss, Using passive multi-modal sensor data for thermal simulation of urban surfaces, ISPRS Annals of the Photogrammetry, Remote Sensing and Spatial Information Sciences (2024). URL: <https://api.semanticscholar.org/CorpusID:270386302>.
- [42] V. Ramani, M. Ignatius, J. Lim, F. Biljecki, C. Miller, A dynamic urban digital twin integrating longitudinal thermal imagery for microclimate studies, Proceedings of the 10th ACM International Conference on Systems for Energy-Efficient Buildings, Cities, and Transportation (2023). URL: <https://api.semanticscholar.org/CorpusID:265007045>.
- [43] L. Evangelisti, C. Guattari, P. Gori, Energy retrofit strategies for residential building envelopes: An italian case study of an early-50s building, Sustainability 7 (2015) 10445–10460. URL: <https://api.semanticscholar.org/CorpusID:8234385>.

- [44] Y. Ham, M. Golparvar-Fard, 3d visualization of thermal resistance and condensation problems using infrared thermography for building energy diagnostics, *Visualization in Engineering 2* (2014) 1–15. URL: <https://api.semanticscholar.org/CorpusID:59455883>.
- [45] M. Tancik, E. Weber, E. Ng, R. Li, B. Yi, T. Wang, A. Kristoffersen, J. Austin, K. Salahi, A. Ahuja, D. Mcallister, J. Kerr, A. Kanazawa, Nerfstudio: A modular framework for neural radiance field development, in: *Special Interest Group on Computer Graphics and Interactive Techniques Conference Conference Proceedings, SIGGRAPH '23*, ACM, 2023. URL: <http://dx.doi.org/10.1145/3588432.3591516>. doi:10.1145/3588432.3591516.
- [46] J. T. Barron, B. Mildenhall, D. Verbin, P. P. Srinivasan, P. Hedman, Mip-nerf 360: Unbounded anti-aliased neural radiance fields, *CVPR* (2022).
- [47] T. Müller, A. Evans, C. Schied, A. Keller, Instant neural graphics primitives with a multiresolution hash encoding, *ACM Trans. Graph.* 41 (2022) 102:1–102:15. URL: <https://doi.org/10.1145/3528223.3530127>. doi:10.1145/3528223.3530127.
- [48] T. Kruczek, Conditions for use of long-wave infrared camera to measure the temperature of the sky, *Energy* 283 (2023) 128466. URL: <https://www.sciencedirect.com/science/article/pii/S0360544223018601>. doi:<https://doi.org/10.1016/j.energy.2023.128466>.
- [49] Flir one pro thermal imaging camera for smartphones | teledyne flir, ????. URL: <https://www.flir.com/products/flir-one-pro/>.
- [50] What is msx?, ????. URL: <https://www.flir.com/discover/professional-tools/what-is-msx/>.
- [51] Flir image extractor cli, ????. URL: <https://pypi.org/project/flirimageextractor/>.
- [52] C. Zhao, L. Zhang, Y. Zhang, All-sky longwave radiation modelling based on infrared images and machine learning, *Building and Environment* 238 (2023) 110369. doi:<https://doi.org/10.1016/j.buildenv.2023.110369>.

- [53] C. Brooke, Thermal imaging for the archaeological investigation of historic buildings, *Remote Sensing* 10 (2018). URL: <https://www.mdpi.com/2072-4292/10/9/1401>. doi:10.3390/rs10091401.
- [54] N. Otsu, A threshold selection method from gray-level histograms, *IEEE Transactions on Systems, Man, and Cybernetics* 9 (1979) 62–66. doi:10.1109/TSMC.1979.4310076.
- [55] A. Horé, D. Ziou, Image quality metrics: Psnr vs. ssim, in: 2010 20th International Conference on Pattern Recognition, 2010, pp. 2366–2369. doi:10.1109/ICPR.2010.579.
- [56] Z. Wang, A. Bovik, H. Sheikh, E. Simoncelli, Image quality assessment: From error visibility to structural similarity, *Image Processing, IEEE Transactions on* 13 (2004) 600 – 612. doi:10.1109/TIP.2003.819861.
- [57] R. Zhang, P. Isola, A. A. Efros, E. Shechtman, O. Wang, The unreasonable effectiveness of deep features as a perceptual metric, in: Proceedings of the IEEE conference on computer vision and pattern recognition, 2018, pp. 586–595.
- [58] M. Tancik, E. Weber, E. Ng, R. Li, B. Yi, J. Kerr, T. Wang, A. Kristoffersen, J. Austin, K. Salahi, A. Ahuja, D. McAllister, A. Kanazawa, Nerfstudio: A modular framework for neural radiance field development, in: ACM SIGGRAPH 2023 Conference Proceedings, SIGGRAPH '23, 2023.